Research article

Priyadharshini Balasubramanian[a], Mathias H. Metsch[a], Prithvi Reddy[a], Lachlan J. Rogers, Neil B. Manson, Marcus W. Doherty* and Fedor Jelezko

Discovery of ST1 centers in natural diamond

https://doi.org/10.1515/nanoph-2019-0148
Received May 19, 2019; revised July 1, 2019; accepted July 2, 2019

Abstract: The ST1 center is a point defect in diamond with bright fluorescence and a mechanism for optical spin initialization and readout. The center has impressive potential for applications in diamond quantum computing as a quantum bus to a register of nuclear spins. This is because it has an exceptionally high readout contrast, and unlike the well-known nitrogen-vacancy center, it does not have a ground state electronic spin that decoheres the nuclear spins. However, its chemical structure is unknown, and there are large gaps in our understanding of its properties. We present the discovery of ST1 centers in natural diamond. Our experiments identify interesting power dependence of the center's optical dynamics and reveal new electronic structure. We also present a theory of its electron-phonon interactions, which we combine with previous experiments, to shortlist likely candidates for its chemical structure.

Keywords: ST1; diamond; color center; spectroscopy; electronic structure.

[a]**Priyadharshini Balasubramanian, Mathias H. Metsch and Prithvi Reddy:** These authors contributed equally to this work.
***Corresponding author: Marcus W. Doherty,** Laser Physics Centre, Research School of Physics and Engineering, Australian National University, Canberra 2601, Australia,
e-mail: marcus.doherty@anu.edu.au
Priyadharshini Balasubramanian, Mathias H. Metsch and Fedor Jelezko: Institute for Quantum Optics, University Ulm, Albert-Einstein-Allee 11, D-89081 Ulm, Germany; and Center for Integrated Quantum Science and Technology (IQST), University Ulm, Albert-Einstein-Allee 11, D-89081 Ulm, Germany
Prithvi Reddy and Neil B. Manson: Laser Physics Centre, Research School of Physics and Engineering, Australian National University, Canberra 2601, Australia. https://orcid.org/0000-0001-9519-6576 (P. Reddy)
Lachlan J. Rogers: Department of Physics and Astronomy and ARC Centre of Excellence for Engineered Quantum Systems (EQUS), Macquarie University, Sydney 2109, Australia

1 Introduction

When designing hybrid quantum technologies, we seek to develop an architecture that uses different types of qubits [1]. The advantage of this approach is that we can exploit each system's strengths while mitigating their weaknesses. By using a hybrid architecture, the diamond quantum computing platform demonstrates impressive performance at room temperature [2]. In particular, these systems use the negatively charged nitrogen-vacancy (NV^-) center's electron spin as a quantum bus to nearby ^{13}C nuclear spins [3–5]. We use this configuration because the electron spin interacts strongly with control fields but is a poor qubit because of its short coherence time. Conversely, the nuclear spins have a long coherence time but cannot be controlled easily because of their weak interactions [6]. One major limitation of this approach is that the NV^- center's ground state electron spins, because its relaxation decoheres the nearby nuclear spins [3, 7]. Efforts have been made to mitigate this problem by electronically switching the NV into a spinless charge state [8]. However, this proves challenging from an engineering perspective.

The ST1 center promises to avoid this issue completely as it has a singlet (spinless) electronic ground state, which allows long nuclear spin coherence, and a photo-excited metastable triplet level, which can realize a quantum bus. The ST1 center also has brighter fluorescence and optical spin-readout contrast than the NV center, making it a strong candidate for the next generation of hybrid diamond quantum computing technologies [9, 10]. However, as the ST1 center's spin must be manipulated in the metastable triplet, its use as a quantum bus is more complicated than the NV center. In particular, initialization must be precisely timed and control pulses must be applied within the lifetime of the state. Furthermore, the triplet's lifetime places a strict upper bound on the spin coherence time, unlike the NV center were dynamical decoupling can be used to extend spin coherence by orders of magnitude.

Progress in utilizing the ST1 center for quantum technology has been frustrated because it has been difficult to reproduce. Indeed, detection of the ST1 center

has only been reported twice: first by Lee et al. [9] in ultra-pure single crystalline HPHT diamond after fabrication of vertical nanowires and later by John et al. [10] in ion-implanted single crystal chemical vapor deposition diamond. As both observations were in manufactured diamond, ST1 creation has been attributed to the synthesis process, and the long-term stability of the defect is unknown. Because of the scarcity of samples, there are large gaps in our understanding of the ST1. Principally, its chemical composition and structure is unknown. Its electronic structure has been partially identified, but it may still have additional levels. There has been no work on studying the ST1 center's electron-phonon interactions or ensemble variation.

In this paper, we report the first observation of ST1 centers in natural diamond, indicating defect stability on geological timescales. We also conducted optical characterization of these ST1 that revealed unknown electronic levels; pump power dependent photodynamics that demonstrate an impressive (up to 80%) optical spin readout contrast at high laser power; and new insight into its electron-phonon interactions that we use to identify the possible chemical structures of the center. These observations provide significantly more insight into the nature of the center, and by shortlisting possible structures, our analysis will enable future studies to be more targeted. This will lead more rapidly to precise identification of the defect.

This paper has the following structure. In section 2, we present an overview of the known characteristics of the ST1. In section 3, we detail the experimental apparatus we used to study our sample. In section 4, we present the optical characterization of the defects found in the sample, including a study of the site-to-site variation of its zero phonon line (ZPL). We then present the photodynamics experiments that demonstrate additional levels in its electronic structure and optical properties. In section 5, we decompose our high-resolution optical spectra to obtain the electron-phonon spectral density. We use this spectral density and critical point analysis in section 6 to identify a set of the simplest possible defect structures that are consistent with experiment.

2 The ST1 center

A few of the key characteristics of the ST1 center are known to date. Lee et al. [9] and John et al. [10] both report that the center's key optical features are a sharp ZPL around 550 nm (2.25 eV) and broad phonon side band (PSB) extending out to 750 nm. These features indicate that the optical transition occurs between two discrete levels deep in the diamond bandgap. Their optical characterization established that it is a single emitter by observing the characteristic dip in photon-autocorrelation at zero delay. The autocorrelation also showed pronounced bunching shoulders, which strongly indicated the presence of a long-lived shelving state.

The proposed electronic structure of the ST1 consists of singlet ground and excited states (see Figure 1). The shelving state was determined to be a triplet. This was demonstrated by observing increased fluorescence corresponding to microwave fields resonant with three electron spin resonance transitions. The increase in fluorescence was explained by studying the optical dynamics of the system. The key features of the optical cycle are a rapid intersystem crossing (ISC) from the excited to the shelving state followed by another ISC to the ground state. The decay rate of the lower ISC is determined by the lifetimes of the triplet sublevels: $\tau_{|0\rangle} \approx 2500$ ns, $\tau_{|-1\rangle} \approx 1000$ ns, and $\tau_{|+1\rangle} \approx 250$ ns. As the $|0\rangle$ state is much longer lived than the other sublevels, the system can be spin polarized into this sublevel. Because of the substantial differences in sublevel lifetimes, the rate of nonradiative decay to ground state via the metastable state can be significantly enhanced when spin population is driven out of the longer-lived triplet sublevels via resonant microwave excitation. This results in an increase in average fluorescence, thereby enabling spin readout and the optical detection of magnetic resonance. The readout contrast is up to 45%.

The optically detected magnetic resonance (ODMR) spectra of the triplets showed a fine structure at zero field: $2E = 278(1)$ MHz, $D - E = 996(1)$ MHz, and $D + E = 1274(1)$ MHz. The spin-Hamiltonian of the triplet manifold is

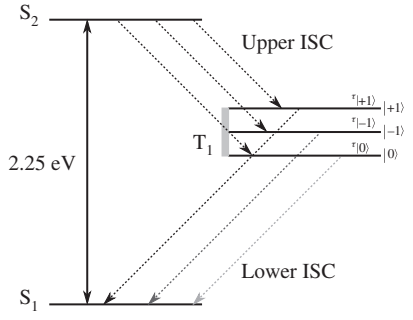

Figure 1: The known electronic structure of the ST1 center. S_1 and S_2 are the ground and excited singlets, respectively. T_1 is the metastable triplet state. The dotted lines indicate the ISCs, and the solid arrow represents the optical ZPL. The lower ISCs are labelled by their depopulation rates, $\tau_{|0\rangle}$, $\tau_{|+1\rangle}$, and $\tau_{|-1\rangle}$.

$$\hat{H} = D\,[S_z^2 - S(S+1)/3] + E(S_x^2 - S_y^2) + \gamma_e \vec{S}\cdot\vec{B} \qquad (1)$$

where $\vec{S} = (S_x, S_y, S_z)$ are the usual dimensionless spin operators, $S=1$ is the total spin, $\vec{B}$ is an external magnetic field, γ_e is the free-electron gyromagnetic ratio (the observed g factor is $g \approx 2.0(1)$), and both $D=1135(1)$ MHz and $E=139(1)$ MHz are the zero field splitting parameters. Rotation of an applied magnetic field demonstrated the spin-quantization axis of the triplet in the ⟨110⟩ crystalline direction; this defines the orientation of the spin operators in equation (1) such that $z \,||\, \langle 110\rangle$. The presence of the E parameter suggests that the center also has a minor spin axis in an orthogonal direction to ⟨110⟩ (e.g., $x \,||\, [100]$, $y \,||\, [011]$, and $z \,||\, [01\bar{1}]$) and that the center has C_{2v} or lower symmetry. Optical polarization studies of the defect show that the transition dipole moment of the main transition is also in ⟨110⟩. However, it is unknown if the spin-quantization axis and dipole moment are co-aligned. Hyperfine splitting of the triplet due to nearby ^{13}C was observed, but no further hyperfine structure intrinsic to the defect was identified. This seemingly suggests that the most prevalent isotopes of the center's chemical constituents are spinless.

3 Experimental details

Our experimental procedure involved identification and analysis of ST1 centers in a natural diamond sample, which was host to a wide verity of fluorescent sites. Our primary tools were optical microscopy, ODMR, optical spectroscopy, and optical dynamics.

For our optical characterization, we employed a home-built confocal fluorescence microscope with a 532 nm green excitation laser. The fluorescence was detected using either an avalanche photodiode or a spectrometer. For our ODMR measurements, we applied microwaves through a copper wire positioned above the sample and an external magnetic field using a permanent magnet. All of our results were obtained at room temperature except our emission spectra, which were obtained at 5 K. For our optical polarization studies, a half wave plate (HWP) along with a linear polarizer was placed in the detection path. Polarization dependence was measured by rotating the half wave plate. Our study of the optical dynamics of the system analyzed the second-order photon correlation function, $g^{(2)}$, at different excitation powers. The autocorrelation function from single sites was measured in a Hanbury Brown and Twiss configuration, where the fluorescence was split by a 50:50 beamsplitter and detected using two avalanche photodiodes.

4 Experimental results

We started by scanning a natural diamond sample using our confocal microscope. As shown in Figure 2A, we find a host of fluorescent sites in the sample. Of these, we observed that many sites increased in fluorescence when we applied microwaves resonant to the known ST1 spin transitions. The sites, marked in Figure 2B, were abundant and uniformly distributed throughout the sample. We identified them as ST1 centers from their emission spectra, depicted in Figure 2E, and ODMR signature, shown in Figure 3A. We repeated magnetic field rotation,

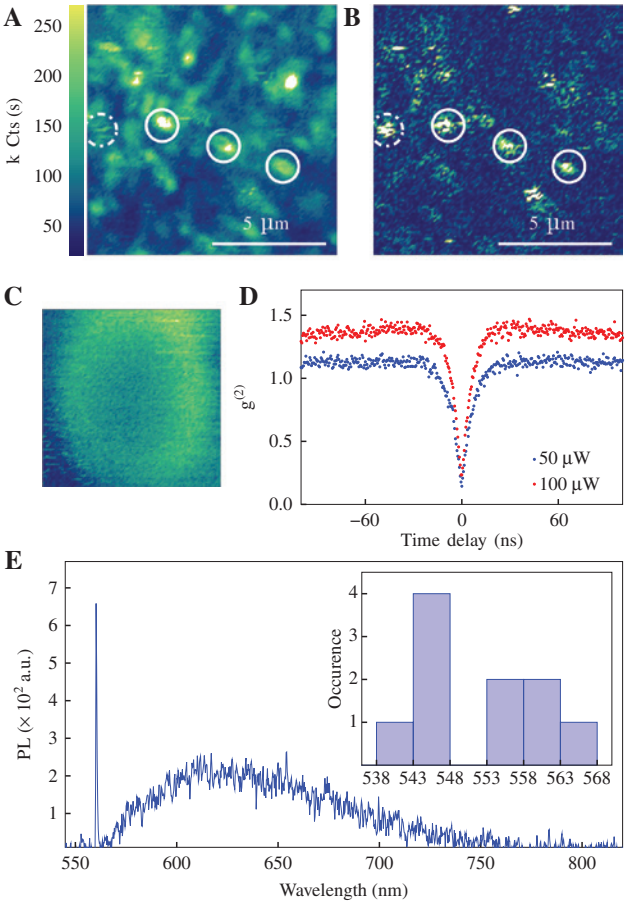

Figure 2: Optical characterization of the ST1 center.
(A) A confocal fluorescence image of the natural diamond sample. The ST1 centers are identified by circles. A solid circle indicates that the center can be spatially isolated from other sources. (B) A confocal fluorescence image of the same region shown in Figure 2A with applied resonant microwaves. (C) Magnified image of a single site at high laser power, showing a doughnut-shaped fluorescence pattern. (D) Normalized photon autocorrelation function measured at different laser power showing anti-bunching at $\tau = 0$. (E) The emission spectra of ST1 at 5 K with a prominent ZPL at 555 nm and PSB extending to 700 nm. The inset depicts a histogram showing the distribution in the position of the ZPL.

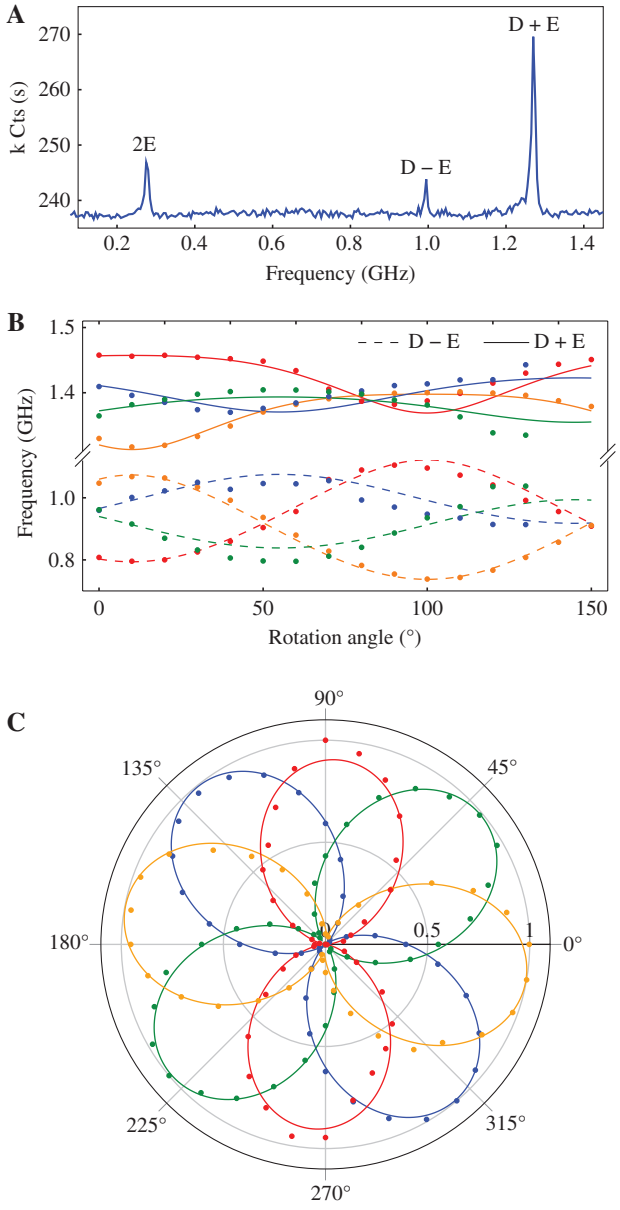

Figure 3: ODMR and optical polarization studies of the ST1 center. (A) ODMR spectrum of ST1 at zero magnetic field. (B) The response of the ODMR frequencies when a $B = 120$ Gauss magnetic field is rotated in the [001] crystal plane. The solid lines represent a fit using equation (1). (C) Plot of the polarization-dependent fluorescence of the ST1 centers. It shows four linear polarization states separated by 45°.

Figure 3B, and polarometry, Figure 3C, to show that the centers have their major spin axis and dipole moment oriented in the ⟨110⟩ directions. However, we could not determine whether these were co-aligned or not. The $g^{(2)}$ autocorrelation for the detected sites, Figure 2D, shows a dip at zero delay and has bunching shoulders at higher excitation powers, which is consistent with the previous observations. We did not observe any hyperfine structure intrinsic to the defect. This supports previous suggestions that the center's chemical constituents are spinless.

We identified 10 sites and studied the variation between ST1 centers from site to site. The spread of the ZPL wavelengths in the sample of centers we measured was ≈20 nm; the ZPL frequency distribution is inset as a histogram in Figure 2E. Notably, each of the defects measured showed similar ODMR spectra. As the ZPL is expected to be significantly more susceptible to strain than the ODMR features, we attribute the distribution of ZPL energies to local variation of strain between sites.

A new feature we observed was an interesting power dependence of the center's photoluminescence. Between laser powers of ≈100 and 200 W, the defect did not show blinking and had a brightness comparable to that of the NV centers. However, as we swept to higher laser powers (up to 800 W), the defects exhibited peculiar saturation behavior. This manifested in a doughnut-shaped fluorescence pattern in our confocal scans, shown in Figure 2C. The dip in fluorescence is due to the Gaussian profile of the laser beam, which only saturates fluorescence as the center of the laser spot passes over the defect. This was further characterized in Figure 4, where we measured total fluorescence while sweeping laser power. As demonstrated in Figure 4C, increasing laser power leads to an impressively higher ODMR contrast of up to ≈80%. These new observations motivated us to revisit of the photodynamics of the ST1 center.

We started with the simplest rate equation model that describes the established electronic structure. This is given by

$$\begin{aligned}
\dot{S}_0 &= -k_{ex}S_0 + k_f S_1 + k_0 T_0 + k_- T_- + k_+ T_+ \\
\dot{S}_1 &= k_{ex}S_0 - k_f S_1 - k_{ISC} S_1 \\
\dot{T}_+ &= \frac{k_{ISC}}{3} S_1 - k_+ T_+ \\
\dot{T}_- &= \frac{k_{ISC}}{3} S_1 - k_- T_- \\
\dot{T}_0 &= \frac{k_{ISC}}{3} S_1 - k_0 T_0
\end{aligned} \tag{2}$$

where excitation from the ground to the excited state is parameterized by k_{ex}, k_f is the excited state's fluorescent lifetime, and the parameters k_+, k_-, and k_0 are the depopulation rates from the respective triplet sublevels. For simplicity, we ignore the differences in the upper intersystem crossings for each triplet, assuming that they are all k_{ISC}. These rates are derived by solving the rate equation and fitting the $g^{(2)}$ autocorrelation; we provide details of this procedure in section Supplementary S1.

We interrogated the power dependence of the rate equation parameters by fitting them at different laser

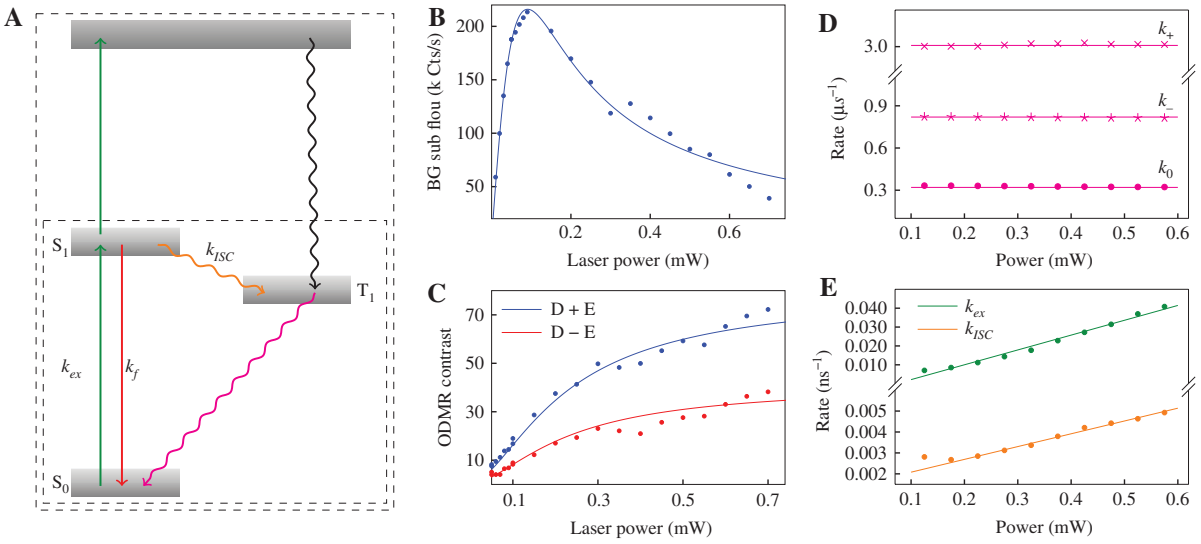

Figure 4: The power dependent optical dynamics of the ST1 center.
(A) A proposed level scheme that could explain the power dependence of the optical dynamics. It includes a second manifold of excited levels that are either internal defect levels or photoionized levels. The remaining subfigures show the optical dynamics as a function of pump power. The solid lines represent a fit using the rate equation model in equation (2). (B) Depicts fluorescence counts. The solid lines represent the fit using the extended rate equation. (C) Shows ODMR contrast. (D) Is the depopulation rates from the triplet levels. (E) Shows optical excitation rate k_{ex} (green) and the upper intersystem crossing rate k_{ISC} (orange).

powers. Figure 4D shows that the depopulation rate from the triplet sublevels is independent of the pump power. This eliminates the possibility of an intensity-dependent depopulation channel from the triplet sublevels to the ground state. Figure 4E depicts the power dependence of k_{ex} (green). As expected k_{ex} increases linearly with pump power, as described by the equation

$$k_{ex} = \frac{\lambda}{hc}\sigma(\lambda)I \tag{3}$$

where I is the applied focal irradiance and $\sigma(\lambda)$ is the corresponding absorption cross-section at excitation wavelength λ. By fitting the slope of k_{ex}, we can extract an absorption cross-section of $\sigma \approx 10^{-17}$ cm^2, which is comparable to the reported absorption cross-section of the NV center.

Figure 4E also shows an unexpected linear dependence of k_{ISC} on pump power (orange). As the upper intersystem crossing rate should be independent of pump power, it suggests that there is another channel for population transfer from the excited state to the triplet. This could be due to an internal transition to an excited manifold of defect levels or photoionization of either an electron to the conduction band or a hole in the valence band. In either case, there needs to be an accompanying preferential decay to the triplet state. Otherwise, the ODMR contrast would also reduce with increasing excitation power, instead of the observed increase. In the case of an internal manifold, this would require an ISC to the triplet state. In the case of photoionization, preferential return to the triplet level could occur via cascaded recapture of the ionized particle, where the particle is captured at a higher rate into the triplet level rather than the ground state because of the emission of fewer phonons. To determine whether the second excited states are internal levels of the defect or ionized states, polarization measurements of the second excitation should be performed. If they are internal states, the second excitation will be well polarized. If they are ionized states, then the excitation will not exhibit polarization. By assuming that the lifetimes of the higher excited states are very small, we can include them phenomenologically into our model (described in section Supplementary S1) to estimate the second excitation rate. From this, we find a second absorption cross-section of $\sigma \approx 10^{-18}$ cm^2.

5 Decomposition of the phonon side band

Focusing now on a detailed analysis of the optical band. The PSB of an optical transition is generated by the electron-phonon interactions involved in the transition. In the absence of vibronic interactions, such as the Jahn-Teller effect, the PSB can be described by the linear symmetric mode model [11]. The linear symmetric mode model was applied extensively by [12] in the analysis of diamond color

centers. Davies showed how the model could be used to extract the electron-phonon spectral density, referred to as the one-phonon band. Applying critical-point analysis allows this spectral density to be interpreted in terms of structural features of the defect [13]. This is the approach adopted in this section.

Given an emission band $I_{em}(\omega)$, the bandshape function, $I(\omega)$, of a center is proportional to $I_{em}(\omega-\omega_0)\omega^{-3}$, where ω_0 is the ZPL frequency and I_{em} is the emission spectra. The band function is given by

$$I(\omega)=e^{-S}I_0(\omega)\otimes\left[\delta(\omega)+\sum_{n=1}^{\infty}\frac{S^n}{n!}I_n(\omega)\right] \tag{4}$$

where S is the total Huang-Rhys factor, I_0 is the ZPL shape, and $\otimes$ denotes convolution. The function

$$I_n(\omega)=\int_{-\infty}^{\infty}I_{n-1}(\omega-x)I_1(x)\mathrm{d}x \tag{5}$$

is the n-phonon band that is constructed by successive convolutions of the one-phonon band. The one-phonon band represents all processes involving the creation and annihilation of a single phonon. Through self-convolutions, it generates the n-phonon band I_n, which describes all n-phonon processes with total energy $\hbar\omega$.

In theory, one can directly extract the one-phonon band from the band function by applying an inverse Fourier transform to equation (4), rearranging to obtain an expression for $I_1(t)$, and then applying a Fourier transform, $\hat{\mathcal{F}}$, to obtain

$$I_1(\omega)=\frac{1}{S}\hat{\mathcal{F}}[\log\ (\hat{\mathcal{F}}^{-1}[I(\omega)-e^{-S}I_0(\omega)])] \tag{6}$$

However, because of the largely featureless PSB of the ST1 center, the large Huang-Rhys factor ($S=5$), and the comparatively low signal-to-noise of our experimental spectra, this direct Fourier deconvolution method is difficult because it is sensitive to numerical and spectral noise. Thus, the direct method is only sufficient to obtain an initial estimate of $I_1(\omega)$.

These issues can be overcome by using an iterative deconvolution method developed by Kehayias et al. [13]. We applied this method by first obtaining an approximate one-phonon band from Fourier deconvolution. We then smoothed and tapered this approximate one-phonon band to form our first estimate $I_1^0(\omega)$ that was appropriately continuous and restricted to $\omega\epsilon[0, \Omega]$, where Ω is the phonon cut-off of diamond. Next, we calculated the normalized PSB components $I_n^0(\omega)$ via successive convolutions of $I_1^0(\omega)$. We applied the following equation to generate an improved estimate $I_1^1(\omega)$ for the one-phonon band:

$$I_1^k(\omega)=e^S I(\omega)-I_0(\omega)-\sum_{n=2}^{\infty}\frac{S^n}{n!}I_0\otimes I_n^{k-1}(\omega) \tag{7}$$

where k is the inductive step index. We then inductively repeated this procedure of calculating the normalized PSB components and generating the next estimate of the one-phonon band until it converged. This processes only required a small number of iterations, and the results are depicted in Figure 5. As can be seen, the generated band function matches the central line of the spectrum very well.

We now turn to critical point analysis to relate the features of the one-phonon band to structural components of the defect. The key assumption of critical point analysis is that the center does not significantly perturb the phonon modes of pristine diamond. Using this approach features in the one-phonon band corresponds to either frequencies of high mode density and/or where there is strong coupling to the defect orbitals. Figure 6 shows the extracted one-phonon band against the phonon band structure (PBS) and density of states (DOS) of diamond. The absence of spectrally sharp features at frequencies above Ω shows that the optical transition does not couple to local modes; only weak coupling to the continuum modes is present. This validates the key assumption of our application of critical point analysis.

As shown in Figure 6, the one-phonon band's largest feature is a broad peak centered at 60 meV. The prominence of this feature indicates that at this frequency, two things are occurring: a high density of modes and strong coupling to the defect. Indeed, the feature is coincident with the "leveling out" of the transverse phonon bands at the L-point, which implies a higher relative density of modes of that phonon type. Furthermore, as the L-point

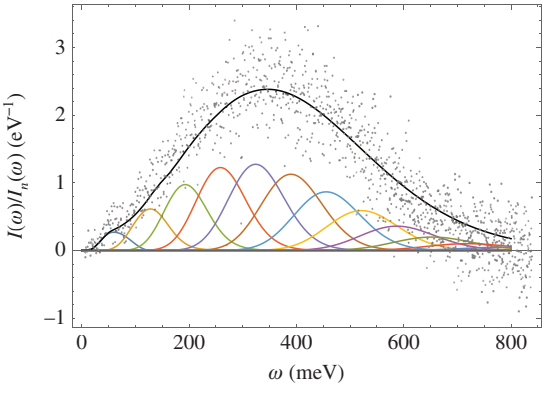

Figure 5: The PSB spectrum from experiment (gray points), a polynomial fit of the spectrum to show its centerline (dashed blue), the calculated PSB (dashed orange), and its constituent n-phonon bands. The sum of n-phonon bands equals the calculated PSB.

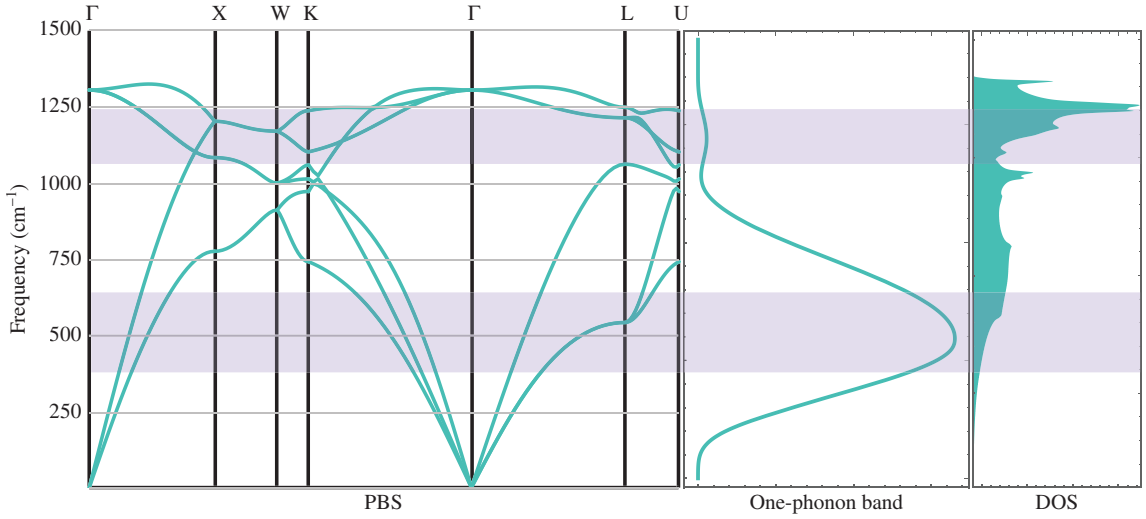

Figure 6: The comparison of the one-phonon band with the DOS and PBS of pristine diamond [14]. The shaded areas connect adjacent points to highlight regions of interest.

lies on the edge of the Brillouin zone, these phonons also result in maximum displacement between equivalent atoms in neighboring unit cells. This implies that for the defect to strongly couple to these modes, its orbitals must be well localized to the nearest-neighbor atoms of a lattice site. This is just like the orbitals of the NV^- center in diamond that surround a vacant lattice site.

The plots in Figure 7 show that the one-phonon bands of ST1 and NV^- are indeed remarkably similar. Assessment of the critical points of the NV^- phonon band by Kehayias et al. [13] showed that it also couples most strongly to phonon modes at the *L*-point. They observed that *L*-point modes would result in the greatest distortion of the electron density localized to the dangling sp^3 orbitals about the center's vacancy. The strong similarities of the one-phonon bands of ST1 and NV^- strongly indicate that the ST1 center contains a vacancy and the orbitals involved its optical transition are highly localized to this vacancy. We use this conclusion to greatly simplify the identification of possible defect structures of the ST1 center.

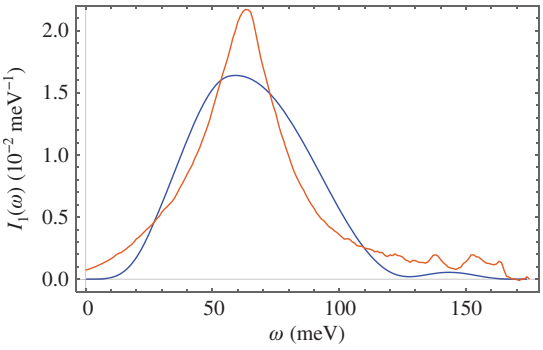

Figure 7: Comparison of the one-phonon bands of the NV^{-1} [13] and ST1 optical transitions.

6 Identifying the ST1

In this section, we outline the simplest defect structures that are consistent with the experimental understanding of the ST1 center acquired to date. The analysis of the PSB motivates studying vacancy centric models for the ST1. Recapping, the center has C_{2v} symmetry or lower, and it is oriented along the [110] axis. These two pieces of information constrain the simplest defect structures to those containing a vacancy with nearby substitutional lattice impurities orientated along the [110] axis. We accordingly restrict the geometries considered in this work to substitutions of either the nearest neighbors to the vacancy or of its next-to-nearest neighbors within the same reflection plane of the defect. Schematics of these geometries are provided in Figure 8.

The shortlisted structures can be further constrained by considering that intrinsic hyperfine structure has not been detected for the ST1 center. As the electron spin density of the defect is localized to the vacancy's nearest-neighbour atoms, the absence of hyperfine structure particularly constrains defects with substitutions of these atoms to those without nuclear spin. Alternatively, a lack of hyperfine would support a next-to-nearest neighbor substitution as spin density would be localized to the vacancy and, thus, unlikely to couple strongly to a nuclear spin two atomic sites distant.

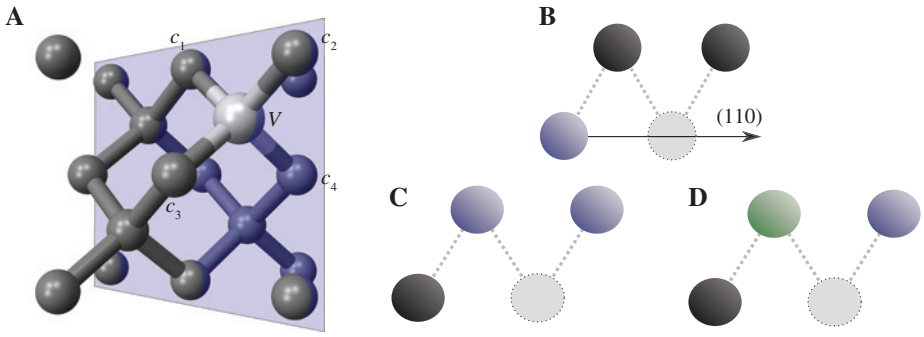

Figure 8: Schematics of the candidate defect structures of the ST1 center.
(A) Is a cell of diamond showing a vacancy and the (110) reflection plane. The other figures are the different possible geometries represented by a (110) cross-section of the defect. If we let *X* and *Y* represent potential impurities, (B) is a next-to-nearest-neighbour substitution, labelled XCV; (C) is the nearest-neighbour substitutions of like atoms, labelled XVX; and (D) is nearest-neighbour substitutions of unlike atoms, labelled XVY.

Table 1: Our selection of the simplest possible candidates for the ST1.

e no.	Defect symmetry and structure		
	C_{1h}	C_{1h}	C_{2v}
4	[Si]*CV*	—	[Si]*V*[Si]
6	[O]*CV*, $[N]^-$	[O]*V*[Si]	—

The labeling convention follows the one defined in Figure 8.

As the ST1 has a ground singlet, it has an integer spin. This means that the defect consists of an even number of electrons. The nearest neighbors to the vacancies contribute at least a total of four electrons to the defect. Impurities may only contribute a total of two additional electrons or none. The defect therefore has either four or six electrons. Ignoring positive charge states because of their low prevalence in diamond, we propose the following candidate impurities: [Si], $[N] + e^-$, and [O] (where [] indicates that it could be any species in the column of the periodic table). We list a selection of the simplest possible ST1 geometries in Table 1.

Having identified the set of simplest defect structures, we will now construct their electronic structures to test if they are consistent with experiment. We do this by applying the standard defect molecule model [15]. Adopting a minimal basis of the four dangling sp^3 orbitals from the atoms surrounding the vacancy, we combine these linearly to form a basis of symmetrized molecular orbitals. Considering a defect with C_{2v} symmetry, we form the following molecular orbitals:

$$\begin{aligned} A_1 &: a_1 = c_1 + c_2 \\ A_2 &: a_1' = c_3 + c_4 \\ B_1 &: b_1 = c_1 - c_2 \\ B_2 &: b_2 = c_3 - c_4 \end{aligned} \tag{8}$$

where c_1 and c_2 are the orbitals centered on the nearest-neighbours atoms in the (110) plane, while c_3 and c_4 are the out-of-plane atoms. A_1, A_2, B_1, and B_2 are the irreducible representations of C_{2v}. Notably, these orbitals are the same as those for a C_{1h} defect. In this case, the symmetry of the A_1 and B_1 states is lowered to A', whereas A_2 and B_2 are lowered to A''.

To proceed with constructing the electronic structure, we must now energetically order the molecular orbitals (MOs). The possible ordering options can be reduced by interpreting the orientations of the center's optical dipole moments and spin quantization axes. The absence of orbital degeneracy in C_{2v} and lower symmetry, combined with the singlet ground state, implies that the highest occupied molecular orbital (HOMO) of the ground configuration is doubly occupied. Hence, we can immediately identify the ground electronic state as a $^1A_1$ via Ünsold's theorem. It follows that the dipole moment of the optical transition and the spin-quantization axes are determined by the levels of the first excited configuration, where one electron has been promoted from the HOMO to the lowest unoccupied molecular orbital (LUMO) of the ground configuration. Lee et al. [9] found that both the dipole moment and the spin-quantization axis are oriented in one of the equivalent [110] directions but could not distinguish if they were co-aligned. In S2, we evaluate the optical selection rules and interpret the elements of the spin-spin tensor to infer the orientation of the dipole moment and spin-quantization axis, respectively. We find that the only HOMO/LUMO pairs that are consistent with experiment are (a_1, b_1) and (a_1', b_2).

The molecular orbital model we present is consistent with the second excited manifold being internal states arising from the occupation of an additional molecular orbital. Though we cannot conclusively show that these are excited states, it is instructive to explore this possibility in the molecular model. Hence, assuming that the

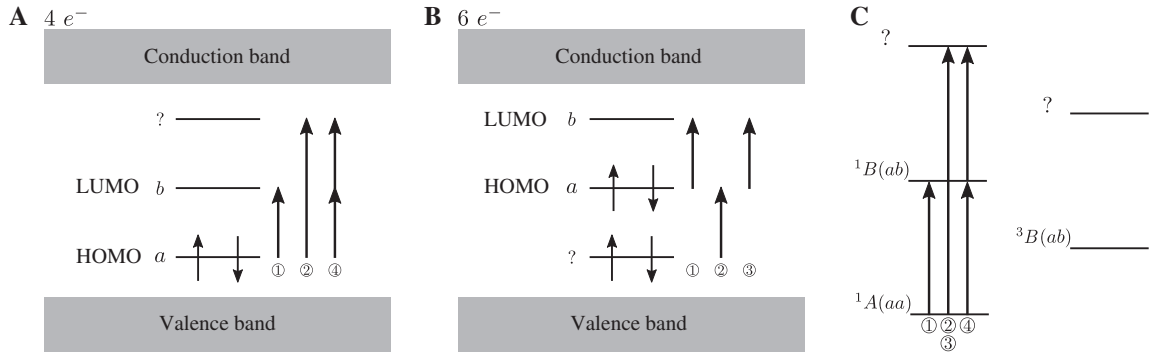

Figure 9: Systematics of the candidate electronic structures of the ST1 center.
For an arbitrary HOMO/LUMO pair (*a*, *b*), (A) and (B) are the potential orbital configurations associated to the four- and six-electron molecular models, and (C) is the associated electronic structure if there was an internal manifold. The numbered arrows represent the allowed transition pathways to the first and second excited transitions. These, when combined with the orientation of the dipole moment, help identify the symmetry of the electronic states.

excited states are internal, observation of a second transition can be used to determine the energetic ordering of the remaining MOs. If the defect comprises of four electrons, the second excited state is where an electron in the HOMO is promoted to the second LUMO. If it has six electrons, there are two potential second excited configurations: (1) where an electron is promoted from the second HOMO to the HOMO (which is partially occupied in the first configuration), or (2) promotion of both the HOMO electrons to the LUMO. Figure 9 shows the MOs and identifies the configurations that could be associated to the excited states. As we did with the first excited state, the transition dipole moment of the second transition can be used to identify the symmetry of the second excited state. Thus, future experimental work should seek to determine the polarization of this second transition to further constrain the possible identity of the molecular orbitals and electronic levels.

Having heavily restricted the large number of defect candidates, it is now feasible to conduct *ab initio* calculations. The electronic structure, transition dipole moment, vertical transition energy, and spin-spin tensor can be extracted from these calculations and compared with the experimental observations and theory presented in our work.

7 Conclusion

In this paper, we report the first discovery of ST1 centers in a natural diamond sample. We present an experimental study of its optical spectra and dynamics, particularly, their dependence on excitation power. We used theoretical tools to identify its possible chemical and electronic configuration. Our key results are as follows: (1) ST1 centers have stability on geological timescales. (2) The centers do not show hyperfine structure intrinsic to the defect. (3) The defect has previously unidentified electronic structure consisting of an excited manifold with an associated transition into the metastable triplet. (4) The ST1 center's spin readout contrast can be enhanced up to 80% by increasing pump power. (5) The absorption cross-section of the first transition is 10^{-17} cm^2. The defect couples most strongly to phonons at the *L*-point, like the NV center. This strongly indicates a vacancy-centered defect. (6) A selection of candidate ST1 chemical structures that are consistent with experiment has been identified in Table S2. (7) The possible ST1 electronic structures that are consistent with experiment have been identified in section 6. These observations are a significant advance in our fundamental understanding of the center. Our work provides the groundwork to make identification of the defect via *ab initio* simulations or experiment feasible. Consequently, it is a significant step toward the practical realization of an ST1 quantum bus.

8 Supplementary material

The supplementary information can be found with the online version of the article.

Funding: This work was supported by funding from the Australian Research Council (DP170103098, DE170100169, DE170101371, and CE170100009). This research was undertaken with the assistance of resources and services from the National Computational Infrastructure (NCI), which is supported by the Australian Government. We also acknowledge support from the DFG (JE 290/18-1 and SFB1279), BMBF

(13N14438, 16KIS0832, and 13N14810), ERC (BioQ319130), VW Stiftung (93432), and Landesstiftung (BW-INT SF III-042).

References

[1] Kurizki G, Bertet P, Kubo Y, et al. Quantum technologies with hybrid systems. Proc Natl Acad Sci USA 2015;112:3866–73.
[2] Waldherr G, Wang Y, Zaiser S, et al. Quantum error correction in a solid-state hybrid spin register. Nature 2014;506:204–7.
[3] Neumann P, Mizuochi N, Rempp F, et al. Multipartite entanglement among single spins in diamond. Science 2008;320:1326–9.
[4] Childress L, Gurudev Dutt MV, Taylor JM, et al. Coherent dynamics of coupled electron and nuclear spin qubits in diamond. Science 2006;314:281–5.
[5] Neumann P, Beck J, Steiner M, et al. Single-shot readout of a single nuclear spin. Science 2010;329:542–4.
[6] Maurer PC, Kucsko G, Latta C, et al. Room-temperature quantum bit memory exceeding one second. Science 2012;336:1283–6.
[7] Filidou V, Simmons S, Karlen SD, Giustino F, Anderson HL, Morton JJL. Ultrafast entangling gates between nuclear spins using photoexcited triplet states. Nat Phys 2012;8:596–600.
[8] Pfender M, Aslam N, Simon P, et al. Protecting a diamond quantum memory by charge state control. Nano Lett 2017;17:5931–7.
[9] Lee S-Y, Widmann M, Rendler T, et al. Readout and control of a single nuclear spin with a metastable electron spin ancilla. Nat Nanotechnol 2013;8:487–92.
[10] John R, Lehnert J, Mensing M, Spemann D, Pezzagna S, Meijer J. Bright optical centre in diamond with narrow, highly polarised and nearly phonon-free fluorescence at room temperature. New J Phys 2017;19:053008.
[11] Maradudin AA. Theoretical and experimental aspects of the effects of point defects and disorder on the vibrations of crystals. Solid State Phys 1966;18:273–420.
[12] Davies G. Vibronic spectra in diamond. J Phys C: Solid State Phys 1974;7:3797.
[13] Kehayias P, Doherty MW, English D, et al. Infrared absorption band and vibronic structure of the nitrogen-vacancy center in diamond. Phys Rev B 2013;88:165202.
[14] Petretto G, Dwaraknath S, Miranda HPC, et al. High-throughput density-functional perturbation theory phonons for inorganic materials. Sci Data 2018;5:180065.
[15] Loubser JHN, van Wyk JA. Electron spin resonance in the study of diamond. Rep Prog Phys 1978;41:1201.

Supplementary Material: The online version of this article offers supplementary material (https://doi.org/10.1515/nanoph-2019-0148).